

Probing the Solar Corona at High Temporal and Spatial Resolution with the LOw Frequency ARray (LOFAR)

Pearse Murphy, B.A. (Mod.)

PhD Transfer Report
School of Physics

Supervisor:

Prof. Peter T. Gallagher

February 2019



Trinity College Dublin
Coláiste na Tríonóide, Baile Átha Cliath
The University of Dublin

Summary

Insert abstract here

Declaration

I have read and I understand the plagiarism provisions in the General Regulations of the University Calendar for the current year, found at: <https://www.tcd.ie/calendar>

I have also completed the Online Tutorial on avoiding plagiarism ‘Ready, Steady, Write’, located at <http://tcd-ie.libguides.com/plagiarism/ready-steady-write>

I declare that this report is my own work, is not copied from any other person’s work (published or unpublished), and has not previously submitted for assessment either at Trinity College Dublin or elsewhere.

Name: Pearse Murphy

Signature: **Date:**

List of Publications

Oral Presentations

1. Thing

Poster Presentations

1. thing

Workshops & Conferences Attended

1. Thing

Publications

1. Ain't none

Contents

List of Publications	iii
List of Figures	vi
1 Introduction	1
1.1 The Sun	1
1.1.1 The Corona	3
1.1.2 Radio Phenomena in the Solar Corona	4
1.1.3 Source Sizes in the Corona	5
1.2 Plasma Emission of Type III Radio Bursts	5
1.2.1 Characteristics of Type III Bursts	6
1.2.2 Sub-categories of Type III bursts	6
1.2.3 Process of Forming Type III Bursts	7
1.2.4 Generation of Langmuir Waves	8
1.2.5 Plasma Emission	9
1.3 Radio Interferometry	11
1.4 Beamforming Theory	11
2 Instrumentation	13
2.1 LOFAR: The LOw Frequency ARray	13
2.1.1 Low Band Antenna	13
2.1.2 High Band Antenna	13
2.1.3 Remote Station Processing Boards (RSPs)	15
2.1.4 Transient Buffer Boards (TBBs)	15
2.2 I-LOFAR: The Irish LOw Frequency ARray	16
2.2.1 Digital Signal Processing for a Single LOFAR Station	16
3 Observation & Data Analysis	19
3.1 Observing High Temporal Resolution	19
3.1.1 The REAL Time Acquisition cluster (REALTA)	19
3.1.2 REALTA Data Analysis	20
3.1.3 The TBB Acquisition Cluster (TACl)	20
3.1.4 TBB Data Analysis	22
3.1.5 Motivation for Study	22

3.1.6	Solar Transient Features	22
3.2	Observing High Spatial Resolution	23
4	Results & Interpretation	27
4.1	TBB Results	27
4.2	Interferometric Results	27
5	Conclusion	31
6	Future Work	32
6.1	Technical Work	32
6.2	Interferometric Analysis	32
6.3	RFI Removal	33
References		34
A	Appendix	35

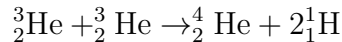
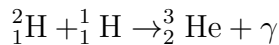
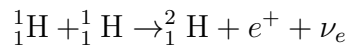
List of Figures

1.1	Diagram of Sun's interior and atmospheric layers.	2
1.2	Model of electron density and temperature with height in the solar atmosphere.	3
1.3	A number of Type III bursts observed by Zucca et al. (2012) on 21 October 2011.	7
1.4	Langmuir wave distribution function and spectral energy density.	9
1.5	A three wave process of fundamental plasma emission $L \rightarrow T+S$	10
1.6	Three wave process of second harmonic plasma emission $L+L' \rightarrow T$	11
2.1	Typical power spectrum for an LBA.	14
2.2	Digital signal processing pipeline of an individual LOFAR station.	17
3.1	Dynamic spectrum of the Sun on January 29th 2019.	21
3.2	Composite of radio spectra from multiple ground and space based radio telescopes.	24
3.3	X-ray flux as measured by the GOES satellite on 2015-10-17	25
3.4	193 Å image of the Sun taken by AIA on 2015-10-17	25
3.5	Type III radio burst observed with LOFAR station RS509	26
4.1	Prototype TBB dynamic spectrum	28
4.2	Prototype TBB all sky image	28
4.3	Interferometric images of a Type III burst at 13:21:55.6 on 2015-10-17 at 4 different frequencies a) 29.68 MHz b) 39.45 MHz c) 49.21 MHz d) 63.28 MHz. The red circle in each panel indicates the size of the Sun and the two red crosses indicate the centre position of the Sun and the position of maximum intensity in each panel.	29

Introduction

1.1 The Sun

The Sun is our nearest star and the centre of our solar system and is a G2 type start located on the main sequence of the Hertzsprung Russell diagram. It has a luminosity of $(3.84 \pm 0.04) \times 10^{26}$ W and a radius $R_{\odot} = (6.959 \pm 0.007) \times 10^8$ m. With a mass of $(1.9889 \pm 0.0003) \times 10^{30}$ kg, it comprises $> 99\%$ of the solar system's total mass (Foukal, 2004). Formed from a cooling cloud of gas and dust 4.6 billion years ago the Sun's core soon reached a temperature of 15MK, thus enabling nuclear fusion to occur. There are a number of nuclear fusion processes in the Sun's core, the most common of which is the proton-proton or 'pp' chain whereby four protons collide and fuse to form a Helium nucleus. The most frequent pp chain is known as ppI, it occurs 86% of the time (Turck-Chièze & Couvidat, 2011) and is as follows,



Here, ${}_1^1\text{H}$ is a proton or Hydrogen nucleus, ${}_1^2\text{H}$ is its isotope Deuterium, ${}_2^3\text{He}$ is the Helium isotope Tritium, ${}_2^4\text{He}$ is Helium, e^+ is a positron, ν_e is an electron neutrino and γ is a gamma ray photon. Each ppI chain releases 4.2×10^{-12} J. The energy output of all pp chains combined account for 98.8% of the total energy produced by the Sun (Turck-Chièze & Couvidat, 2011).

Photons generated in the ppI travel outwards from the core however, their small mean free path of 0.9cm means that this takes on the order of 10^5 years to reach the solar surface (Mitalas & Sills, 1992). At 70% of the Sun's radius ($0.7R_{\odot}$), the temperature has cooled to 1MK thereby allowing electrons to bind to atomic orbitals, drastically decreasing the scattering rate of photons. Energy transfer from here to the solar surface at $1R_{\odot}$ is now primarily done through convection. The layer of the Sun at $1R_{\odot}$ is known as the photosphere and is what would be called the surface of the Sun. This is the point at which the optical depth for visible light photons is 1 and their mean free path is much greater than the distance between scattering centres on the solar surface. Above the photosphere is the Sun's atmosphere consisting of the chromosphere, transition region and the corona. Figure 1.1 shows the interior layers of the Sun and its atmosphere.

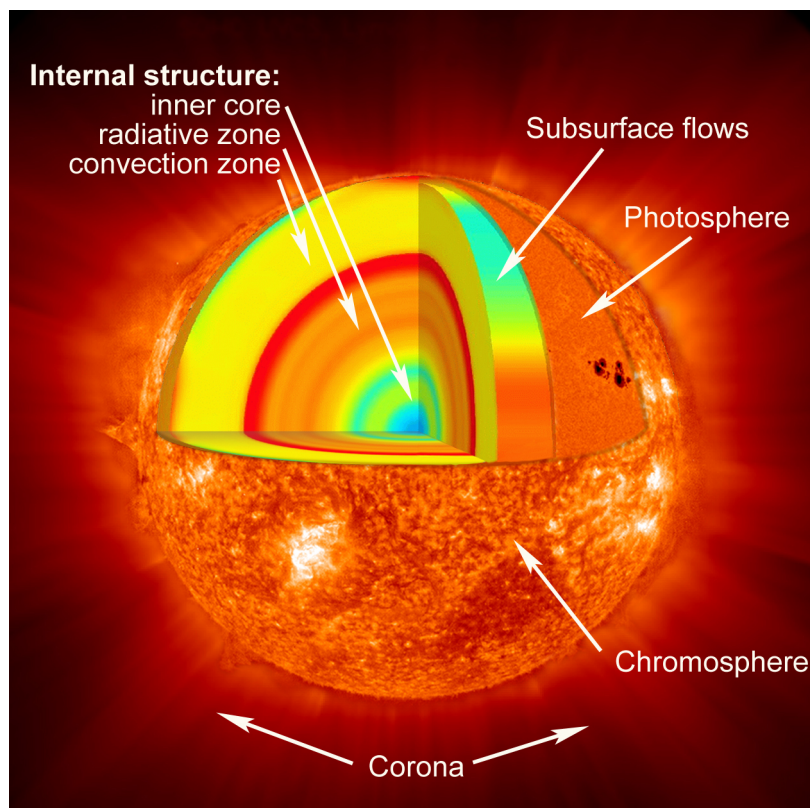


Figure 1.1: Diagram of Sun's interior and atmospheric layers. Photons produced by nuclear fusion in the core transfer energy outwards through the radiative zone to $0.7R_{\odot}$. At this point, convection becomes the main form of energy transport. The visible surface of the Sun is known as the photosphere and marks the boundary between the interior and the atmosphere. The solar atmosphere consists of three layers, the chromosphere, the transition region (not shown) and the corona.

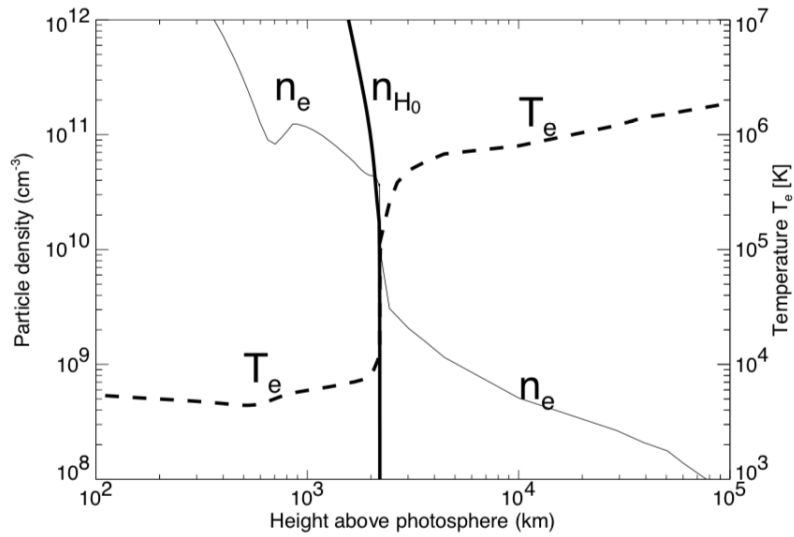


Figure 1.2: Model of electron density and temperature with height in the solar atmosphere. The region around 2000km showing a sharp rise in temperature and sharp fall in electron density is known as the transition region, above this height plasma becomes fully ionised. Image taken from Aschwanden (2004)

1.1.1 The Corona

The outermost layer of the solar atmosphere is called the corona. It is a hot, tenuous plasma which displays a number of interesting phenomena thought to be governed by its complex magnetic field. The corona begins $\sim 2500\text{km}$ above the photosphere after a layer in the Sun's atmosphere known as the transition region, where electron density decreases and temperature increases dramatically. The electron density in the corona ranges from 10^9 cm^{-3} at the base to 10^6 cm^{-3} at distances of $1R_\odot$ from the solar surface. Coronal densities can vary depending on the magnetic field geometry with sparse, under dense regions known as coronal holes or areas where magnetic activity is high known as active regions exhibiting an order of magnitude greater electron density.

Historically, the corona could only be observed during total solar eclipses as the emission from the corona due to Thompson scattering is far less intense than emission from the photosphere. Observing the white light corona is now done with a number of instruments on board space craft orbiting the Sun called coronagraphs, that emulate the effect of a total eclipse. The Large Angle and Spectrometric Coronagraph (LASCO) C2 coronograph is one such instrument and allows the corona to be observed out to distances of $32R_\odot$. This has lead to an increase in observations of structures known as coronal streamers and the phenomenon of coronal mass ejections. Due to its extreme temperature, the corona is easily visible in extreme ultraviolet (EUV) light and is observed in many different passbands with instruments such as the Atmospheric Imaging Assembly (AIA) on board the Solar Dynamics Observatory (SDO). During solar flares, coronal loops fill with hot plasma

and begin to emit in soft X-rays. At the same time, electrons are accelerated towards the solar surface where their energy is converted to hard X-rays in the collision. These X-Ray observations of the corona have been taken by the Reuven Ramaty High Energy Solar Spectroscopic Imager (RHESSI).

Some of the most energetic phenomena in the solar system occur due to magnetic field configurations in the corona. Solar flares, coronal mass ejections and solar energetic particles all involve the acceleration of particles into the heliosphere and can often impact Earth. Studies of these phenomena have been carried out across the electromagnetic spectrum however the main interest in this PhD is radio phenomena.

1.1.2 Radio Phenomena in the Solar Corona

The solar corona is the location of a number of not fully explained radio phenomena. These include the “classic” Type I-V radio bursts described by Wild (1950) which have been linked to features and events in the solar atmosphere i.e., active regions and coronal shocks (Dulk, 1985; Nelson & Melrose, 1985). There are a wealth of other radio bursts observed in the corona, predominantly found in radio storms such as S bursts, drift pairs and stria (McConnell, 1980; Melrose, 1982; Nelson & Melrose, 1985). Understanding the temporal and spatial structure of these bursts help us understand more about particle acceleration and energy release in the solar corona and may give insight into the coronal heating problem.

A brief description of some of the faster solar radio phenomena is given here while a more in depth review of the emission process for Type III bursts and their subcategories is given in section 1.2.

S bursts S bursts, initially called Fast Drift Storm (FDS) bursts, were first observed at the Culgoora Solar Observatory in 1967 (Ellis, 1969) They were later renamed by McConnell (1980) who likened them to Jovian S bursts. They have a narrow bandwidth of the order of 0.03 MHz and a drift rate of $1\text{-}2 \text{ MHz s}^{-1}$ and durations much less than 1s. McConnell (1980) also concluded that S bursts are radiated at either the plasma frequency or its harmonic in a manner similar to Type III bursts, see section 1.2, but that the implications of S burst fine structure and coronal scattering can only be defined once it is determined which harmonic of the plasma frequency they are radiated at. Melnik et al. (2010) propose a model of S bursts being generated by coalescence of fast magnetosonic waves with Langmuir waves which agrees well with the analysis of Clarke et al. (2019). Modern observations of S bursts, such as those conducted using LOFAR’s tied-array imaging mode (Morosan et al., 2015), can give greater insight into the spectral and temporal variability of S bursts and what this might mean for the environment they are generated in.

1.1.3 Source Sizes in the Corona

Analysis of short temporal bursts with small bandwidths suggest source sizes in the corona to be of the order ~ 6000 km (McConnell, 1980). Radio images of the Sun at metric and decametric wavelengths have yet to reveal this level of spatial structure. This is mostly due to the limit of resolution obtainable with modern interferometers however, the suggestion that there is a fundamental limit imposed upon the level of resolution obtainable by scattering in a turbulent corona (Bastian, 1994) has gathered a following in recent years (Kontar et al., 2017). Riddle (1974) described the effect of scattering in a spherically symmetric corona with random isotropic inhomogeneities with and without density enhancements due to streamers. Here they showed that the “directivity pattern”, the ratio of the power received from a source with and without scattering, was significantly broadened for radio bursts near the local plasma frequency, 80 MHz in their case.

Sub arcminute interferometric observations of Type III radio bursts could give a definitive answer to this question.

1.2 Plasma Emission of Type III Radio Bursts

In 1942 while Britain was on the look out for radar signals of enemy aircraft, a strong, noise like and highly variable signal was noticed by radar operators. Initially it was thought that Germany had managed to learn the secret of radar and create some sort of jamming device. On further investigation it was found that this jamming was in fact radio emission from the Sun. The discovery of this radio emission being associated with a major solar flare was kept secret until after the war and was published by Appleton & Hey (1946). Since then a number of major advancements in both instrumentation and theory have occurred. A culmination of the theory of solar radio emission is laid out in the book by McLean & Labrum (1985) while worldwide, a number of extraordinary radio telescopes and interferometers such as the LOw Frequency ARray (LOFAR, van Haarlem et al. 2013), the Nançay Radio Heliograph and the Murchison Widefield Array (MWA), to name but a few, have been built.

Solar radio emission often comes in the form of bursts of varying timescales. These were initially classified into three types by Wild & McCready (1950) with a fourth and fifth type being discovered by Boisshot & André (1957) and Wild et al. (1959) respectively. Of these, the most frequently occurring are the so called Type III radio bursts. These are short bursts that can be observed over many frequencies and are found to be associated with solar flares (Malville & M., 1962). An initial study into how they are emitted was conducted by Ginzburg & Zhelezniakov (1958).

1.2.1 Characteristics of Type III Bursts

Reid & Ratcliffe (2014) review a number of notable properties of Type III bursts. The defining characteristic of Type III bursts is a drift from high to low frequencies in a dynamic spectrum. The drift rates for Type III bursts are typically quite fast, of the order of $\sim 10 \text{ MHz s}^{-1}$. The frequency drift rate, df/dt , has been found to have various relations with frequency (Reid & Ratcliffe, 2014) but most agree that $df/dt \propto f^\alpha$, where α varies depending on the study from ~ 1 to ~ 2.7 .

Ginzburg & Zhelezniakov (1958) proposed that Type III bursts are emitted at the plasma frequency,

$$\omega_p^2 = \frac{n_e e^2}{m_e \varepsilon_0} \quad (1.1)$$

where n_e is the number density of electrons, m_e is the electron mass, e is the electron charge and ε_0 is the permittivity of free space. Although Eq. 1.1 is relatively simple, it contains an important principle of plasma physics. Namely, the plasma frequency is proportional to the square root of the electron density. This means that plasmas at higher electron densities will oscillate at higher frequencies than those of lower densities. The drift in Type III bursts, which are emitted at ω_p , is therefore an indication of the emission source moving from an area of high electron density, the photosphere, to low density, the upper corona.

Type III bursts are often observed to be in two bands, a fundamental and harmonic band that are emitted at ω_p and $2\omega_p$ respectively. Both bands exhibit the same frequency drift although the flux of the harmonic band is usually less than that of the fundamental band. The process of plasma emitting radio frequencies at ω_p and $2\omega_p$ will be explained in more detail in section 1.2.5.

Figure 1.3 shows Type III radio bursts below 400 MHz observed by Zucca et al. (2012). A Type II burst was also observed between 140 and 330 MHz and exhibits a much slower frequency drift than the Type III bursts. A Type III storm can be seen below 200 MHz. This is when Type III emission is continuous over the span of large time scales and can last days.

1.2.2 Sub-categories of Type III bursts

There are different subcategories of Type III bursts. These include: reverse and bi-directional bursts, Type IIIb bursts, U and J bursts.

Reverse and bi-directional bursts A typical Type III burst is produced when an electron beam travels along a magnetic field line away from the Sun to areas of lower density. During the magnetic reconnection process that accelerates these electrons, some electrons travel into the Sun to areas of higher density and thus have a reversed frequency

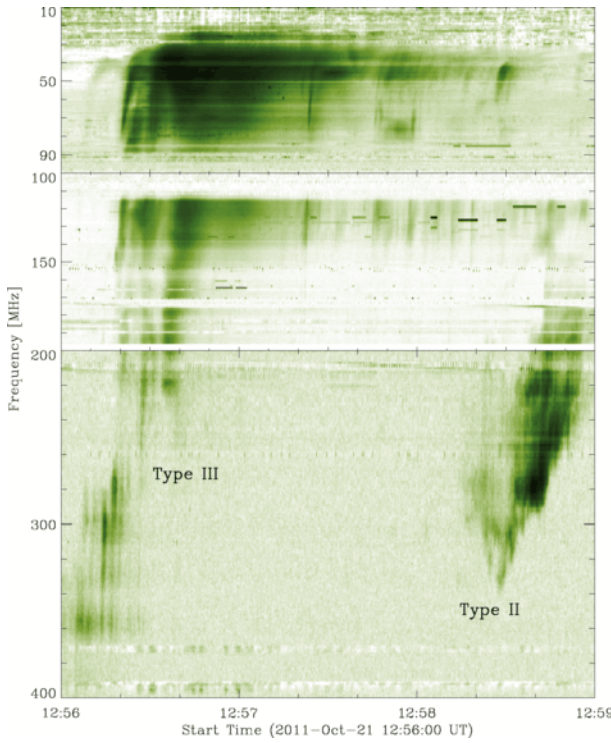


Figure 1.3: A number of Type III bursts observed by Zucca et al. (2012) on 21 October 2011. Note the Type III storm below 200 MHz and the Type II burst between 140 and 330 MHz.

drift. Bursts where both the regular and reverse drifts can be seen simultaneously are bi-directional bursts.

Type IIIb bursts While typical Type III bursts have smooth emission, Type IIIb bursts contain a fragmented substructure. This substructure is in the form of a chain of emission bands/striae that drift in frequency as a whole but individually show little frequency drift.

Type U and J bursts In the case where electrons are travelling along a closed magnetic field line, a turning point in the frequency drift of a Type III burst can be observed. For electrons that generate radio emission down to the footpoint of the magnetic field line, a U burst is observed. A U burst can be identified as an inverted U on a dynamic spectrum. More often, electrons stop generating radio emission as they travel back down the magnetic field line so only the turning point in frequency drift is visible in dynamic spectra. These are known as J type bursts. The reason for higher occurrence of J bursts compared to U bursts is described by Reid & Kontar (2017).

1.2.3 Process of Forming Type III Bursts

For a Type III radio burst to be emitted, an electron must generate Langmuir waves in the plasma. These Langmuir waves then go on to generate electromagnetic transverse

waves by coalescing with other waves or by decaying. These electromagnetic waves are the radio bursts that are observed. In this section the generation of Langmuir waves and the process of plasma emission are discussed.

1.2.4 Generation of Langmuir Waves

During magnetic reconnection in a solar flare electrons are accelerated along magnetic field lines. As these beams of electrons propagate, faster electrons begin to outpace slower electrons and stationary ions in the background plasma. This leads to a second peak on the Maxwell Boltzmann distribution of velocities. The positive velocity gradient means that there are electrons with velocities greater than the phase velocity, v_ϕ . As a result of this, energy is transferred from the electrons to Langmuir waves but because there are more electrons with velocity greater than v_ϕ than there are electrons with velocities less than v_ϕ (where energy is transferred from the wave to the particles), this causes Langmuir waves to become unstable and their magnitudes to grow exponentially. Particles with velocities near v_ϕ are in resonance with the Langmuir waves and drive this instability.

This instability is alleviated by what is known as quasi-linear relaxation (Melrose, 1987) whereby the resonant behaviour of the electrons and Langmuir waves results in a plateau in the Maxwell Boltzmann distribution rather than a second peak. It can be shown that (Vedenov, 1963) the electron distribution function, $f(v, t)$ where $\int f(v, t)dv = n_e$, and the spectral energy index of Langmuir waves, $W(v, t)$ such that $\int W(v, t)dv = E_L$ the total energy density, can be expressed as follows,

$$\frac{\partial f(v, t)}{\partial t} = \frac{4\pi^2 e^2}{m_e^2} \frac{\partial}{\partial v} \frac{W}{v} \frac{\partial f(v, t)}{\partial v} \quad (1.2)$$

$$\frac{\partial W(v, t)}{\partial t} = \frac{\pi\omega_p}{n_e} v^2 W \frac{\partial f(v, t)}{\partial v} \quad (1.3)$$

Equation 1.3 shows that the growth rate of Langmuir waves is proportional to $\frac{\partial f(v, t)}{\partial v}$, hence a positive gradient in the Maxwell Boltzmann distribution leads to a growth in Langmuir waves. The right hand side of Eq. 1.2 has a diffusion operator $D = \frac{W}{v}$. This states that the transfer of energy from particles to waves and back leads to the distribution function being smoothed out and eventually becoming a plateau. The evolution of $f(v, t)$ and $W(v, t)$ with time is shown in Figure 1.4. Figure 1.4 shows how the plateau in the distribution function and a broadening in the spectral energy density develop as time progresses.

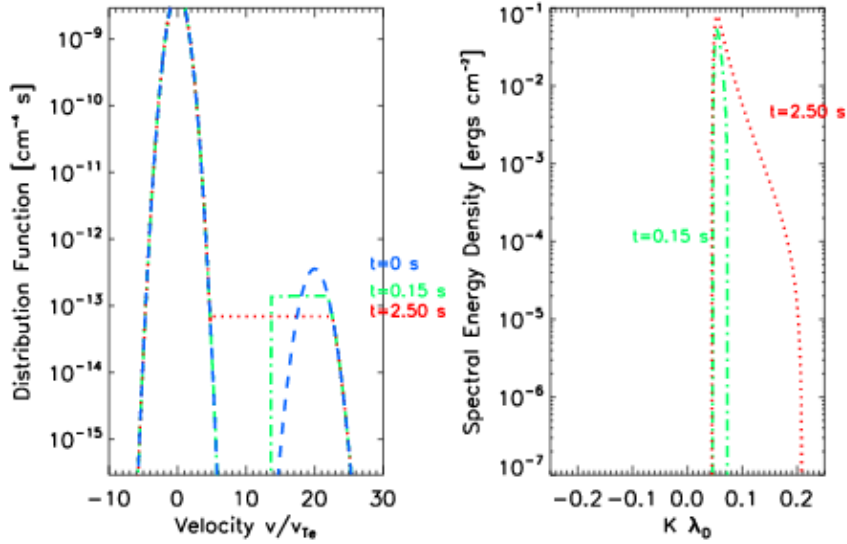


Figure 1.4: Left: Evolution of distribution function (normalised by the electron thermal velocity $v_{T_e} = V_e$) in time. The diffusive term in 1.2 causes the bump-on-tail Gaussian to turn into a plateau, thereby eliminating the instability caused by the positive velocity gradient. Right: The spectral energy density of generated Langmuir waves, x-axis normalised to the Debye length $\lambda_D = \sqrt{\frac{e_0 k_B T_e}{e^2 n_e}}$. As time passes the spectral range of Langmuir waves increases. Each panel shows successive times of $t=0.15\text{s}$ (green, dot-dashed line) and $t=2.50\text{s}$ (red, dotted line). (Figure taken from Reid & Ratcliffe, 2014).

1.2.5 Plasma Emission

In plasma emission the magnetic field of the plasma can be neglected because it only plays a small part in the emission process. As such, only three types of waves need to be considered: transverse (T) waves, Langmuir (L) waves and ion sound (S) waves. These have the respective dispersion relations,

$$\omega = (\omega_p^2 + k^2 c^2)^{\frac{1}{2}}$$

$$\omega \cong \omega_p + \frac{3k^2 V_e^2}{2\omega_p}$$

$$\omega = k v_s$$

where V_e is the thermal velocity of electrons in the plasma, v_s is the ion sound speed and k is the wave vector. Only transverse waves with $\omega > \omega_p$ can escape and thus a plasma emission mechanism is a process that generates these transverse waves.

As mentioned in Section 1.2.1, Type III bursts have a harmonic structure associated with plasma emission at the plasma frequency and the second harmonic. Both of these transverse waves are formed in different three wave processes that will now be discussed. In a plasma, due to scattering from other wave modes and ions in the plasma, a wave

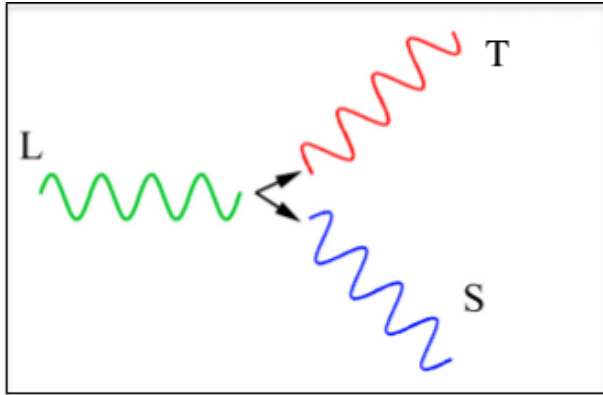


Figure 1.5: A three wave process of fundamental plasma emission $L \rightarrow T + S$. A Langmuir wave decaying into an ion sound wave and an electromagnetic transverse wave at the plasma frequency. (Figure adapted from Solar (interplanetary) Radio Bursts: the Generation of Radio Waves, an oral presentation by David Malaspina at the Jean Louis Steinberg International Workshop on Solar, Heliospheric and Magnetospheric Radioastronomy, November 2017)

mode can be changed from one to the other. This is expressed in the equation

$$\sigma \rightleftharpoons \sigma' + \sigma''$$

where σ , σ' and σ'' represent different wave modes. Conservation of energy and momentum state,

$$\omega^\sigma(k) = \omega^{\sigma'}(k') + \omega^{\sigma''}(k'')$$

$$k = k' + k''$$

where $\omega^\sigma(k)$ is the frequency of a particular wave mode with the wave vector k . For Langmuir (L), ion sound (S) and transverse (T) wave modes the allowed processes are $L+S \rightarrow L'$, $L+S \rightarrow T$, $T+S \rightarrow L$, $T+S \rightarrow T'$ and $L+L' \rightarrow T$. Of these $L+S \rightarrow T$, $L \rightarrow T+S$ are responsible for fundamental emission while harmonic emission is associated with the three wave process $L+L' \rightarrow T$.

Originally Ginzburg & Zhelezniakov (1958) considered fundamental emission to be due to Langmuir waves scattering off of thermal ions in the plasma. It is now commonly accepted that the biggest cause of fundamental emission is due to the three wave processes of a Langmuir wave coalescing with an ion sound wave generated by $L \rightarrow L'+S$ or when a Langmuir wave decays into an ion sound wave and an electromagnetic transverse wave. The process $L \rightarrow T+S$ can be visualised as in Figure 1.5. In solar radio physics it is often assumed that $k_L \gg k_T$, knowing this and that the wave vectors must satisfy $\mathbf{k}_L \pm \mathbf{k}_s = \mathbf{k}_T$ (+ for $L+S \rightarrow T$, - for $L \rightarrow T+S$) implies $\mathbf{k}_s \approx \mp \mathbf{k}_L$

Second harmonic emission occurs when two Langmuir waves coalesce in the process $L+L' \rightarrow T$, shown in Figure 1.6. Conservation of momentum requires that $\mathbf{k}_L + \mathbf{k}'_L = \mathbf{k}_T$ and for second harmonic (H) generation, $k_T = k_H \approx \frac{\sqrt{3}\omega_p}{c}$. The phase speed v_ϕ of Langmuir waves is much less than $\frac{c}{\sqrt{3}}$ meaning that $k_L \gg k_T$ which results in $\mathbf{k}_L \approx -\mathbf{k}'_L$.

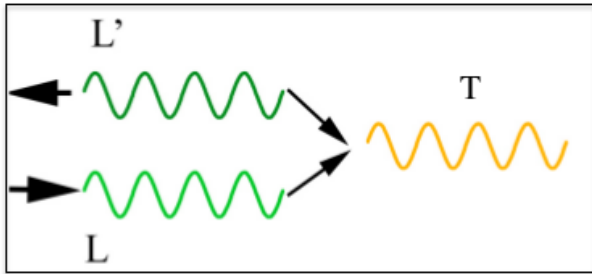


Figure 1.6: Three wave process of second harmonic plasma emission $L+L' \rightarrow T$. A Langmuir wave (L) and a backwards propagating Langmuir wave (L') coalesce to form a transverse wave (T) at $2\omega_p$. (Figure adapted from Solar (interplanetary) Radio Bursts: the Generation of Radio Waves, an oral presentation by David Malaspina at the Jean Louis Steinberg International Workshop on Solar, Heliospheric and Magnetospheric Radioastronomy, November 2017)

This means that for a transverse wave at the second harmonic to be created, two Langmuir waves must coalesce almost exactly head on. These backward propagating Langmuir waves are generated: in the three wave processes of $L+S \rightarrow L'$ and $L \rightarrow L'+S$; scattering off of thermal ions; and refraction at density inhomogeneities.

1.3 Radio Interferometry

Ever since Galileo perfected the telescope in 1609, astronomy has been limited by simple diffraction (and to a greater extent, atmospheric conditions). Rayleigh's criterion states that for an object to be resolved, the maximum of its interference pattern must overlap the minimum of another. This leads to the mathematical relationship,

$$\theta = \frac{\lambda}{D}$$

where θ is the angular resolution of an object, λ is the wavelength observed in and D is the aperture diameter of the telescope. Hubble Space Telescope with a diameter of 3m and observing in near IR therefore, has an angular resolution of ~ 0.05 arcseconds. For a radio telescope observing 10m waves to have the same resolution, ignoring atmospheric effects, it would need an aperture diameter of 41000km. Building a single dish of this size is practically impossible. Fortunately, because radio waves are so large, their phase information ,as well as intensity, can be recorded. Thus, multiple, smaller radio antenna placed at great distances will obtain the same resolution as a single dish.

1.4 Beamforming Theory

In it's most simple terms, beamforming means pointing a phased array such as LOFAR in a particular direction. It involves correcting for phase difference between the “phase centre” of the beam and the position of the source of interest for each baseline and then

summing it all together. Beamforming in a LOFAR station is done by the RSP boards (section 2.1.3) in a matter of seconds however, in order to utilise TBB data (section 2.1.4), this must be done in post processing which can take considerably longer.

The *phase centre* of an array is the direction the primary beam is pointing in. For a moveable dish, this is wherever it is aimed on the sky. For a stationary, phased array this is zenith. The coordinate system commonly used throughout radio interferometry is the l,m,n or directional cosine coordinate system. This determines a position on the sky in terms of the direction cosines to that position. Here l,m and n are defined as

$$l = \cos \delta \sin \Delta\alpha$$

$$m = \sin \delta \cos \delta_0 - \cos \delta \sin \delta_0 \cos \Delta\alpha$$

$$n = \sqrt{1 - l^2 - m^2}$$

where δ, δ_0 are the declinations of an object and the phase centre, respectively, and $\Delta\alpha = \alpha - \alpha_0$ is the difference between the right ascension of the object and phase centre.

The next set of relevant coordinates is what is known as the *uvw* coordinate system. This is a representation of where a particular baseline exists in wavelength space. It is defined as

$$\begin{bmatrix} u \\ v \\ w \end{bmatrix} = \frac{1}{\lambda} \begin{bmatrix} \sin H & \cos H & 0 \\ -\sin \delta \cos H & \sin \delta \sin H & \cos \delta \\ \cos \delta \cos H & -\cos \delta \sin H & \sin \delta \end{bmatrix} \begin{bmatrix} B_x \\ B_y \\ B_z \end{bmatrix}$$

Here, H is the hour angle of an object, δ is its declination, $\mathbf{B} = (B_x, B_y, B_z) = (x_2 - x_1, y_2 - y_1, z_2 - z_1)$ is the baseline or distance between two antennae and λ is the wavelength of the radio light being observed.

In order to beamform, one must account for the phase difference between the phase centre (where the beam is physically pointing) and the source (at an angular coordinate of (l,m) with reference to the phase centre). This phase difference for a baseline pq is given by

$$\kappa_{pq} = 2\pi(u_{pq}l + v_{pq}m + w_{pq}(n - 1))$$

In order to correct for the phase difference and steer the beam, data for baseline pq is multiplied by the complex weight $e^{-i\kappa_{pq}}$, this is repeated for all baselines and finally all data is summed.

Instrumentation

2.1 LOFAR: The LOw Frequency ARray

The LOw Frequency ARray (LOFAR, van Haarlem et al. 2013) is a radio interferometric array spread across Europe. The first LOFAR core station was completed in 2008. Since then, LOFAR has continued to grow to 40 stations in the Netherlands alone with a further 13 across the rest of Europe and 2 more stations planned for completion in 2019/20. Along with the addition of new stations, an extensive set of software for imaging, calibration, RFI flagging and more has been written for use with data produced by LOFAR. Imaging pipelines described in van Haarlem et al. (2013) have also been developed to further maximise the quality of the sub-arcsecond spatial resolution data LOFAR can provide with its full ~ 2000 km baseline. Every LOFAR station is connected to the CEntral Processor cluster (CEP) located in Groningen in the Netherlands by 10Gbps fibre optic cable where data is beamformed and correlated by the COrelator and Beamformer Application for the LOFAR Telescope, a GPU based cluster designed with commerical components (Broekema et al., 2018).

LOFAR observes radio electromagnetic radiation at frequencies of 10-240MHz in two bands, 10-90MHz and 110-240MHz. The gap between the two bands is included in order to avoid observing in the noisy FM band which is dominated by commerical radio broadcasting. To observe in each band, two different antenna designs are utilised, the Low Band Antenna (LBA) for 10-90MHz and the High Band Antenna (HBA) for 110-240MHz.

2.1.1 Low Band Antenna

The LBA consists of two lengths of copper wire which act as a cross dipole antenna, allowing measurements from two linear polarisations. These are connected to a preamplifier placed on top of a PVC pipe. Each wire is 1.38m long which results in a 52MHz resonance peak however, due to the impedance of the amplifier this is increased to 58MHz. A typical LBA power spectrum is shown in Figure 2.1. The LBA is attached to a steel ground plane made out of concrete reinforcement rods, which acts as a reflector for radio light, by synthetic rubber straps and polyester rope. The simple design of the LBA and the fact that it observes at such low frequencies means that it is sensitive to the entire sky at once and digital beamforming techniques can be used to form a beam at any part of the sky within seconds.

2.1.2 High Band Antenna

The higher end of the spectrum is observed by the HBA. The HBA design is drastically different to the simple design of the LBA in order to reduce system noise. One HBA

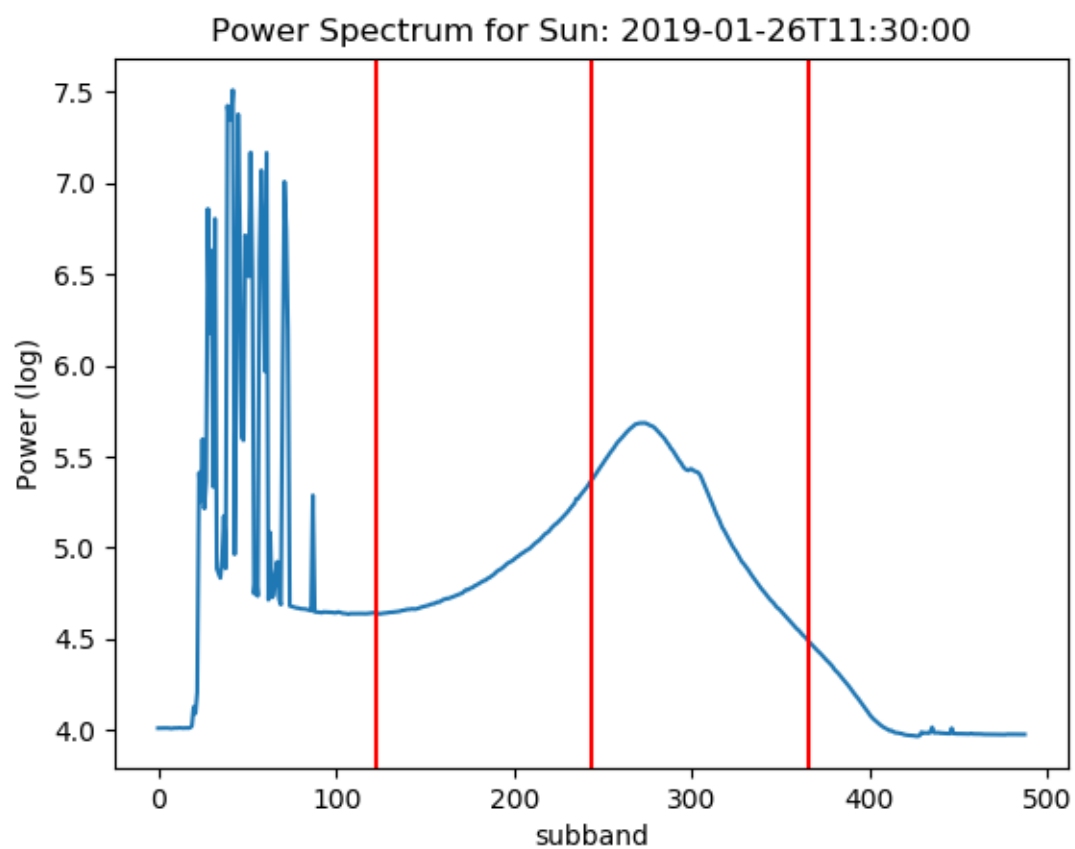


Figure 2.1: Typical power spectrum for an LBA.

is a 5m x 5m tile consisting of 16 bow-tie cross dipole antennae all aligned in the same direction supported in an expanded polystyrene structure. The HBA sits on top of a 5cm × 5cm wire mesh ground plane and is encased in two overlapping polypropylene foil layers in order to protect it from the weather. Each bow-tie antenna in a HBA tile is connected to a front-end which performs preamplification and analogue beamforming, using lengths of copper. Each front-end is then connected to a summator where all the signals are summed before being sent for further signal processing in the station container (Section 2.2.1).

2.1.3 Remote Station Processing Boards (RSPs)

The Remote Station Processing Boards (RSPs) perform all digital signal processing in a LOFAR station. Each LOFAR station consists of 24 RSP boards capable of channelising, beamforming and correlating raw voltage data recorded by either the LBAs or HBAs. A polyphase filter converts recorded data into 1024 complex subband signal which, because the signal is real, is fully described by the positive 512 subbands. These 512 subbands offer $\sim 195\text{kHz}$ frequency resolution across the band. In order to perform beamforming, each RSP is connected together in a ring. Data is passed along this ring and summed in each RSP where a phase correction is also applied in order to “point” the telescope beam. A maximum of 488 subbands can be used to create beamlets, beams pointed in a particular direction observing in a particular frequency. Data from this process is streamed to an external storage node from 4 points in the ring (from 4 RSPs) each containing one quarter of the beamlets computed by the RSP boards.

2.1.4 Transient Buffer Boards (TBBs)

One of the lesser used pieces of LOFAR hardware are the Transient Buffer Boards (TBBs). TBBs are RAM buffers that can temporarily store data at its natively sampled 5ns time resolution. Each LOFAR station contains a total of 12 TBBs ranging from 1 GB to 32GB of memory. More recently completed stations such as the Irish LOFAR station (I-LOFAR) have 32GB TBBs while the older Dutch stations usually have less than 16GB. A 32GB TBB can store up to 5 seconds worth of data recorded by a LOFAR station although this can be increased if fewer inputs or polarisations are recorded. TBBs are currently used in analysing cosmic ray showers and lightning storms but have yet to become a mainstream tool for solar physics, despite their potential. Recording the radio Sun at 5ns has never been attempted before and as such could offer a wealth of never before studied phenomena or cast new light onto longstanding questions. While the next generation telescopes like the Square Kilometre Array (SKA) and the Murchison Widefield Array (MWA) sample at higher rates than 5ns, none of them store full time resolution data. This gives LOFAR

the unprecedeted abiltiy to capture transient events at their highest temporal resolutions yet.

2.2 I-LOFAR: The Irish LOw Frequency ARray

One of the many benefits to using LOFAR as a radio telescope is that each station can be used independently in Single Station Mode which, in the case of international stations, gives freedom to the host countries to make specific observations that may not be covered in a LOFAR observing cycle. Not only this but Single Station mode offers the flexibility of the raw complex voltage data before it has passed through any averaging or calibration pipelines that occur during international observing mode.

This allows direct access to raw voltage data meaning any form of data processing imaginable can be performed. The only limit to this is the computer power and data storage available, two extremely non-trivial problems with LOFAR data. Recording complex raw voltage data from the RSPs requires a 10Gbps fibre optic link between the LOFAR cabinet and a powerful computer cluster. Due to the unpredictable nature of solar radio bursts, the only way to guarantee they will be recorded is to observe for many hours. Data quickly become terabytes in size which becomes challenging to perform any amount of post-analysis. Another disadvantage of using Single Station mode is that, because the main appeal of LOFAR are its long baseline capabilities, little has been developed for Single Station use which only has a maximum baseline of $\sim 300\text{m}$ however, for spectral work this is less of an issue.

The Irish LOFAR station was completed in July of 2017 and is one of the only stations that is used during single station mode to predominantly observer the Sun. A great effort has been made by members of the I-LOFAR consortium, in particular the staff and students of the solar physics research group in Trinity College Dublin / Dublin Institute for Advanced Studies, to utilise I-LOFAR to its fullest potential, collaborating with Griffin Foster of the Breakthrough Foundation to develop a real time transient detection computer cluster and software suite and Dr. Brian Coghlan from the School of Computer Science and Statistics to capture data from the TBBs. In order to fully understand the challenges posed by recording data in singal station mode, the digital signal processing pipeline for I-LOFAR should be explained.

2.2.1 Digital Signal Processing for a Single LOFAR Station

The LOFAR digital signal processing pipeline for a single station is outlined in Figure 2.2. Analogue signal is received by the High Band Antennas (HBAs) or Low Band Antennas (LBAs). This is sampled at 200,000,000 samples per second and converted to a digital signal by a 12 bit A/D converter inside the station's Receiver Units (RCUs). Each RCU

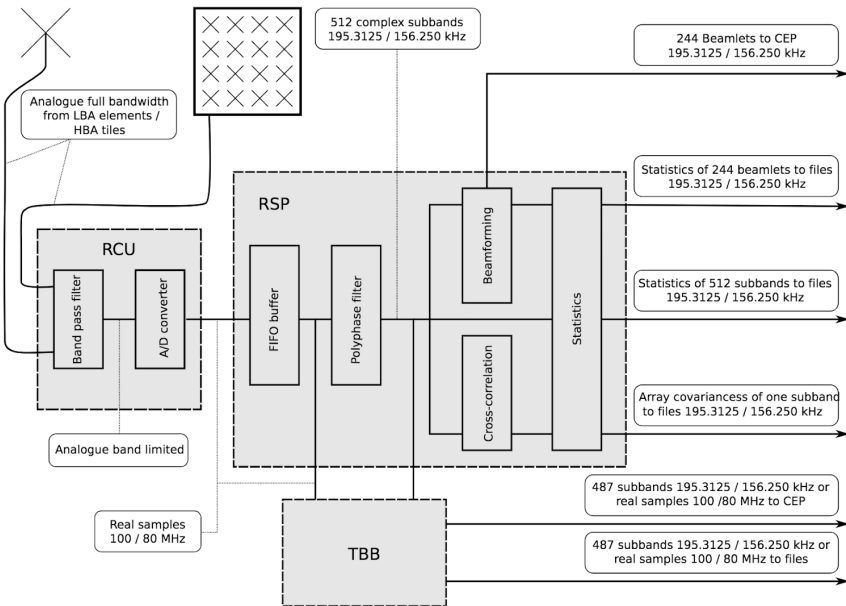


Figure 2.2: Digital signal processing pipeline of an individual LOFAR station. Data is first digitised in the ReCiever Unit (RCU) before being sent to the RSP board. Here data is channelised by a polyphase filter and beamformed before being sent to the CEntral Processor (CEP) in the Netherlands. Also featured is the TBB which stores data in a ring buffer unless it is read out to an external storage system.

digitises data for 1 antenna feed (X or Y polarisation) so there are $96 \times 2 = 192$ RCUs in total. The digitised data is then sent to the Remote Station Processing boards (RSPs). In a standard LOFAR observation while the station is in International LOFAR Telescope (ILT) mode, data from 8 RCUs are channelised into 512 subbands by a polyphase filter bank. This results in raw complex voltage data at 195.3125kHz frequency resolution and $5.12\mu\text{s}$ temporal resolution which are then phase shifted and added together in order to “beamform” to a particular location on the sky. The output from each of the 24 RSP boards are added in a ring before being sent along a 10Gbps fibre link to Groningen and passed into the COBALT processing cluster where the data can be further channelised and correlated to produce interferometric or beamformed data products. The digital signal processing pipeline is much the same in Single Station Mode however, data is averaged out to 1 second before being saved as various “statistics” files. These include subband statistics, which give the power spectrum for each antenna; beamlet statistics, give the power in each beamlet formed by the LOFAR station; and crosslet statistics, the correlation coefficients between each antenna which can be used to create all sky images. Parallel to this, the raw voltage signal with the full 5ns temporal resolution is stored in the memory of a TBB. A single LOFAR station has 12 TBBs which take 2 RSP boards as inputs each. The buffer will constantly overwrite itself until it is frozen and dumped either by an internal/external trigger signal or sending a dump command manually.

The drastic reduction of 6 orders of magnitude temporal resolution when a station is

in Single Station Mode is the main motivation for I-LOFAR to develop its own computer clusters for the storage and processing of single station data. Alongside this, a dedicated storage node for TBB data will enable I-LOFAR to store its highest time resolution data which has many uses because you have a much finer frequency resolution too, and you can keep the same time resolution if you don't care how long it takes to run the simulations.

Observation & Data Analysis

This chapter describes observational efforts with I-LOFAR in single station mode along with an overview of the telescope backends being used to carry out the observations. An interferometric observation of a Type III radio burst is also described.

3.1 Observing High Temporal Resolution

The major problem in radio astronomy currently is the computing power necessary to analyse the enormous amounts of data generated. For example, one hour of observation with I-LOFAR results in 1.3 TB of data being recorded. In order to record high temporal data from I-LOFAR, two computer clusters have been developed in the Rosse Observatory in Birr, The REAL Time Acquisition cluster (REALTA) and the TBB Acquisition Cluster (TACl). Both clusters are connected to I-LOFAR via 10Gbps fibre optic cable and record data from the RSPs and TBBs respectively. Once recorded, the challenge of analysing vast amounts of data remains. Software to display simple previews of data has been developed and efforts are underway for a more efficient solution.

3.1.1 The REAL Time Acquisition cluster (REALTA)

REALTA is a 6 node computer cluster designed specifically to perform high speed de-dispersion on incoming RSP data in order to search for fast radio transients. The physical hardware has been in place since August 2018 and first light data was obtained on September 21st 2018. Despite being designed for fast radio transients, it is also useful for observing other astrophysical phenomena with high temporal variability such as solar radio bursts and pulsars. The hardware for REALTA was purchased predominantly by University College Cork while a storage node and uninterruptible power supply were supplied by National University of Ireland, Galway. The head node is provided by the Breakthrough Listen initiative. Table 3.1 shows the hardware specifications for the different nodes that make up REALTA.

The core computing power of REALTA comes from its 4 Dell PowerEdge R740XD servers. These each have 32 CPU cores, 256GB of RAM and an NVIDIA Tesla V100 16G GPU. This makes REALTA ideal for powerful, parallel computing tasks. In its current state, data is recorded to one compute node where it is analysed afterwards however, we are currently in collaboration with Griffin Foster from the Breakthrough Foundation to implement computer code that utilise REALTA's 4 powerful GPUs in order to analyse data as it is recorded.

Table 3.1: Table of hardware specifications for REALTA

Node Function	Compute Node	Storage Node	Headnode
CPU	Intel Xeon Gold 6130	Intel Xeon E5-2640	Intel Xeon Silver 4110
CPU Clock Speed	2.10GHz	2.40GHz	2.10GHz
No. CPU Cores	64	40	32
RAM	256GB	256GB	93GB
Storage	68TB (total, February 2019)	128TB	N/A
GPU	16GB NVIDIA Tesla V100	N/A	N/A

3.1.2 REALTA Data Analysis

To date, some of the only data recorded with REALTA have been pulsar observations as part of a Very Long Baseline Interferometry (VLBI) pulsar observation campaign. Solar observations were made during the time of a C5 class flare on January 29th. Unfortunately, this was a radio quiet event and the spectrum showed little of interest. Figure 3.1 shows the dynamic spectrum recorded from 11:30 UTC on 2019-01-26.

3.1.3 The TBB Acquisition Cluster (TACl)

TACl is a 6 node computer cluster dedicated to the recording and storage of I-LOFAR TBB data. TACl consists of 4 Dell PowerEdge SC1425 servers, an Isilon IQ 9000X storage server and an Isilon IQ 36NL storage server. TBB data is recorded to TACl solely by the Isilon IQ 9000X storage server. This is configured in RAID6 in order to write incoming UDP (User Datagram Protocol) packets containing TBB data to disk. This storage server has 12 disk slots, 8 of which contain Hard Disk Drives (HDDs) that write and store the incoming TBB data at $\sim 300\text{MB/s}$. The remaining 4 slots house 2 disks containing the operating system and 2 Solid State Drives (SSDs) which are being tested as replacements for the HDDs due to their faster data writing speed.

The Isilon IQ 36NL storage server is intended as general purpose for both TACl and REALTA. It has space for 36 HDDs and has been tinkered with to get over the 1TB per HHD limit. Currently most of this storage server is empty containing only one 1TB HHD and 2 OS disks. Due to the fact that Ubuntu OS and mdraid do not limit storage size, the total possible storage capacity for the Isilon IQ 36NL storage server is $34 \times 1, 2, 4, 8, 16\dots\text{TB}$.

The Dell PowerEdge SC1425 servers are currently unused but are intended for light data post-processing or could possibly act as a buffer for incoming TBB data using a similar idea to LOFAR's best effort buffer.

Detailed hardware specifications of each server in TACl are shown in Table 3.2.

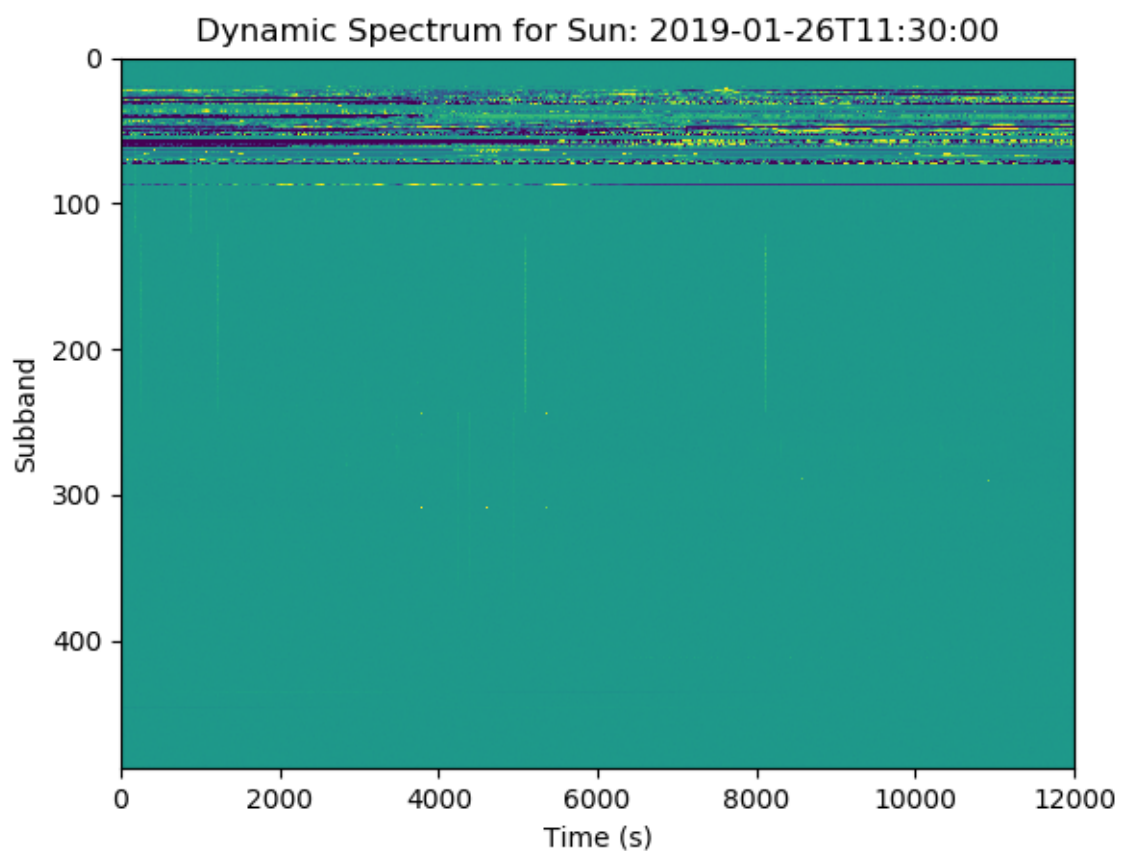


Figure 3.1: Dynamic spectrum of the Sun on January 29th 2019. A solar flare occurred at 13:21 (6660s since observation start) however no radio activity was detected.

Table 3.2: Table of hardware specifications for TACl

	Isilon IQ 9000X	Isilon IQ 36NL
CPU	Intel Xeon E5335	Intel Xeon E5410
CPU Clock Speed	2.00GHz	2.33GHz
No. CPU Cores	4	4
RAM	1GB	4GB
Storage	48TB	1TB

3.1.4 TBB Data Analysis

Initial work in this PhD was centred around obtaining the highest temporal resolution observations of the Sun to date. The task was to use I-LOFAR’s TBBs to constantly monitor the Sun and to output when something of interest occurred. Unfortunately, this task requires a lot of technical knowledge and an adequate computer and network set-up, neither of which were present. Regardless, software to beamform data from TBBs was developed and a TBB correlator was utilised to produce prototype dynamic spectra and all-sky images.

3.1.5 Motivation for Study

The study of radio emission from the Sun, Type III bursts in particular, is just as active now as it was immediately after WW2. New instruments like LOFAR and MWA are being used in various ways to observe and study Type III bursts and their sub-categories (McCauley et al., 2017; Morosan et al., 2014; ?). The study of Type III bursts give us an insight into the magnetic reconnection that takes place during solar flares. This has implications in space weather research which can have widespread effects here on Earth.

With new discoveries being made on a regular basis, long disputed questions are being answered and new questions are being asked. The development of the next generation of radio interferometers, the Square Kilometre Array (SKA), will hopefully bring about a new world of information on Type III bursts and the plasma processes that generate them.

3.1.6 Solar Transient Features

One of the goals of this PhD is to use REALTA and TACl to observe a number of solar transient features at the highest resolution to date. Current progress on TACl has been slow due to technical problems in TBB data capture and REALTA is operational in a minimal sense however, both show enormous potential for the future. Recent publications on Sbursts, TypeIIIBs and many more show that there is much to be learned if we just had the resolution!

3.2 Observing High Spatial Resolution

The second aspect of thesis PhD is to study high spatial resolution observations of the Sun. One of the fundamental questions about solar radio observations is: are source sizes what they are observed to be or does scattering in the corona have a major effect? Interferometric observations from LOFAR are one of the best methods of testing this hypothesis, especially if the remote and international stations can be used to generate the longest baselines resulting in sub arcminute and even sub arcsecond resolution.

In order to learn more about fine structural scale in the corona and the degree to which scattering effects radio emission, an interferometric dataset of a Type III radio burst is being analysed. The data is taken from 17/10/2015 using all of the core LOFAR stations and 12 of the remote stations, a total of 36 stations, yielding 630 baselines with a maximum of 84km. The Type III burst occurred at 13:21 UTC and can be seen in the composite radio spectra in Figure 3.2 .was not co-temporal with any other solar event.

Xray flux around the time of the Type III burst was measured by the Geostationary Operational Environmental Satellite (GOES, seen in Figure 3.3). It should be noted that there were a number of small C class solar flares before the radio burst however none were co-temporal.

EUV images of the Sun such as those taken in the 193Å channel with AIA, Figure 3.4, show a number of bright active regions and a coronal hole which give indications of where to expect closed and open magnetic field lines.

A spectrum of the Sun was recorded using the LOFAR remote station RS509 from 2015-10-17 08:00 UTC to 2015-10-17 14:00 UTC. The Type III burst is observed in this spectrum approximately 19300s after the observation start as shown in Figure 3.5a. Figure 3.5b shows the burst over a shorter time scale thus allowing the variability in emission to be seen.

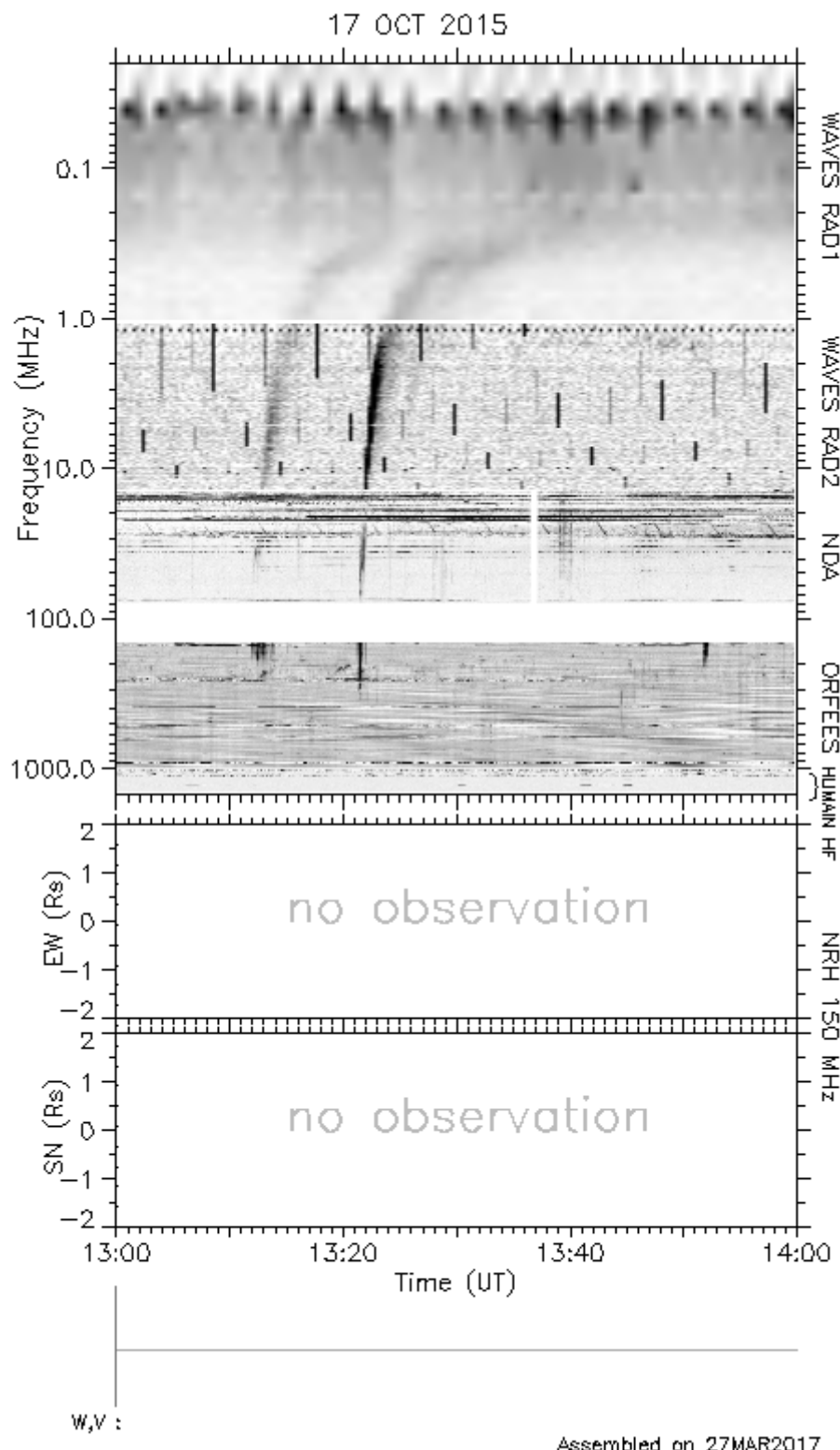


Figure 3.2: Composite of radio spectra from multiple ground and space based radio telescopes. From top to bottom these include; WAVES RAD1, WAVES RAD2 (both on board the WIND space craft), the Nançay Decametric Array (NDA), ORFEES radio-spectrograph (Observations Radio pour Fedome et l'Etude des Eruptions Solaires) and the Nançay Radio Heliograph (NRH, no data). A Type III radio burts is seen as a dark streak after 13:20 in all 4 spectra.

3.2 Observing High Spatial Resolution

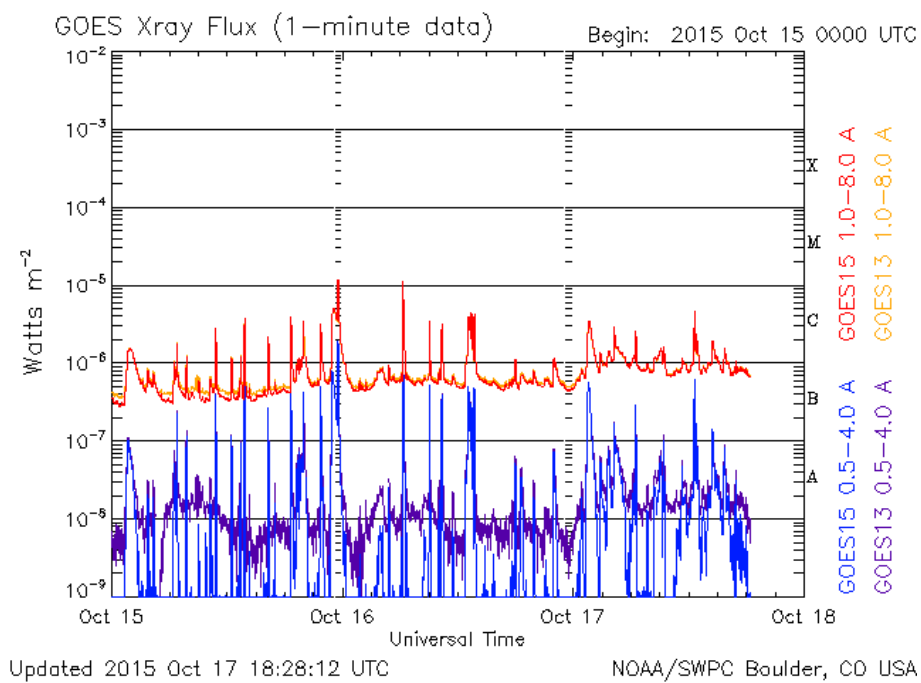


Figure 3.3: X-ray flux as measured by the GOES satellite on 2015-10-17

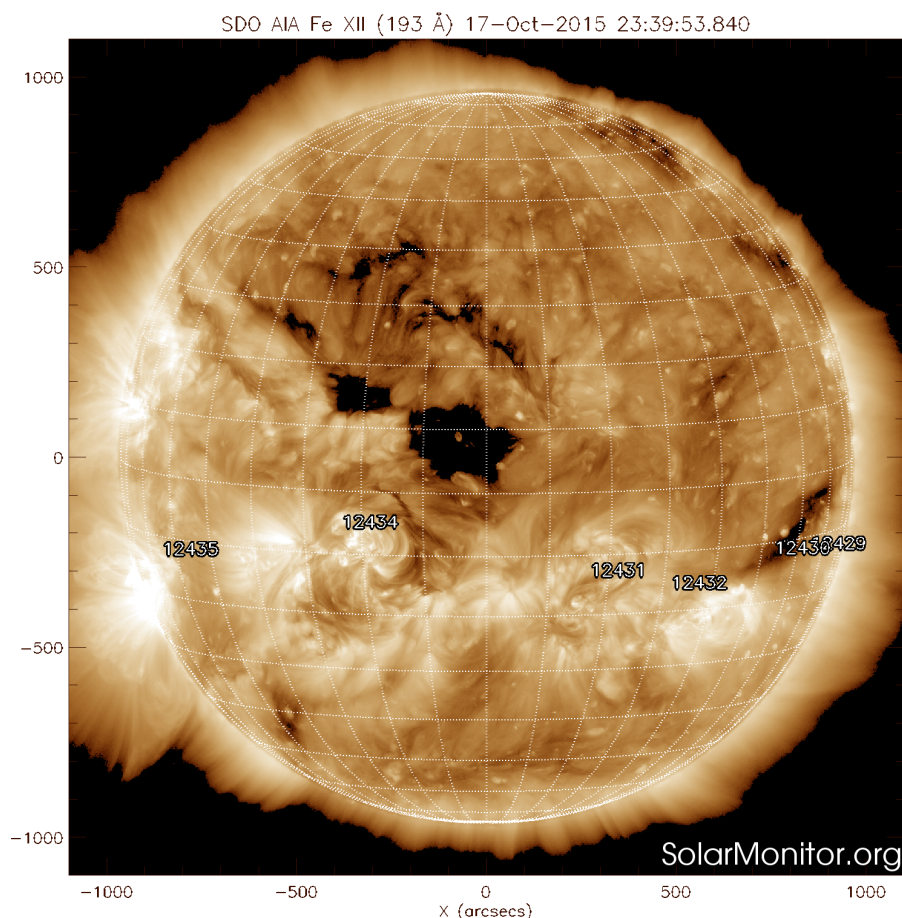


Figure 3.4: 193 Å image of the Sun taken by AIA on 2015-10-17

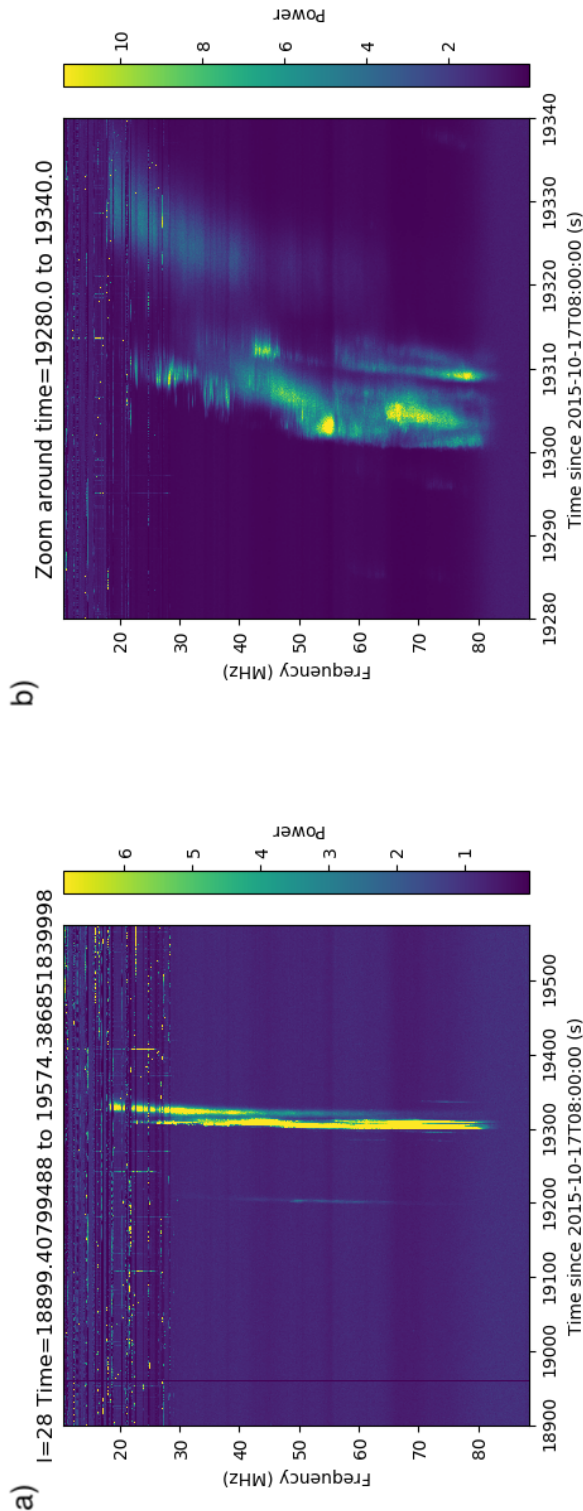


Figure 3.5: a) Type III radio burst observed with LOFAR station RS509 in the north of the Netherlands. b) A zoom in of the Type III burst, a plethora of temporal and frequency variation can be seen over the burst's duration.

Results & Interpretation

Initial results from TBB observations are described here along with preliminary images of a type III burst.

4.1 TBB Results

The initial work during this PhD was done on building a data analysis pipeline for TBB data from I-LOFAR. At the time, TAC1 (section 3.1.3) was still in its early stages of operation and testing of data acquisition method indicated much more needed to be done to capture TBB data at a sufficient rate. Despite this, a moderate codebase (https://github.com/ILOFAR/TBB_scripts, described in Appendix A) was created in order to analyse this “commissioning data”. This software allows TBB data to be beamformed in any direction on the sky to produce a dynamic spectrum such as the prototype dynamic spectrum of the Sun in Figure 4.1. Following a number of technical challenges and set backs, development of this code has since dropped in the list of priorities of this PhD however, it is expected to be revisited once analysis of an interferometric observation of a Type III burst (section 3.2) is complete.

A correlator for TBB data (<https://github.com/sabourke/tbb-correlator>) was utilised to produce the prototype all sky image of Figure 4.2. In order to correlate data correctly, all input data must have the exact same start time. This criteria was only fulfilled by 7 antennas leading to poor uv coverage and a point spread function or beam with numerous sidelobes, this in turn produced the low quality image shown.

Once TAC1 can record TBB data reliably, development and implementation of the existing code can continue. It is hoped that by the end of this PhD that “quick look” plots of TBB data can be produced in almost real time as the data is being recorded in order to automatically discern whether there is an event of interest or if the data can be deleted. It is expected that a number of machine learning algorithms will be utilised in this process.

4.2 Interferometric Results

Figure 4.3 shows a number of preliminary interferometric images at different wavelengths of the Type III burst described in section 3.2. Here, 4 subbands corresponding to 29.68, 39.45, 49.21 and 63.28 MHz of the burst are displayed. The red crosses in each panel indicate the centre of the Sun and the point of maximum intensity in the burst, the red circle show the size of the Sun. The Type III source can be seen at a greater distance from the Sun with decreasing frequency as expected.

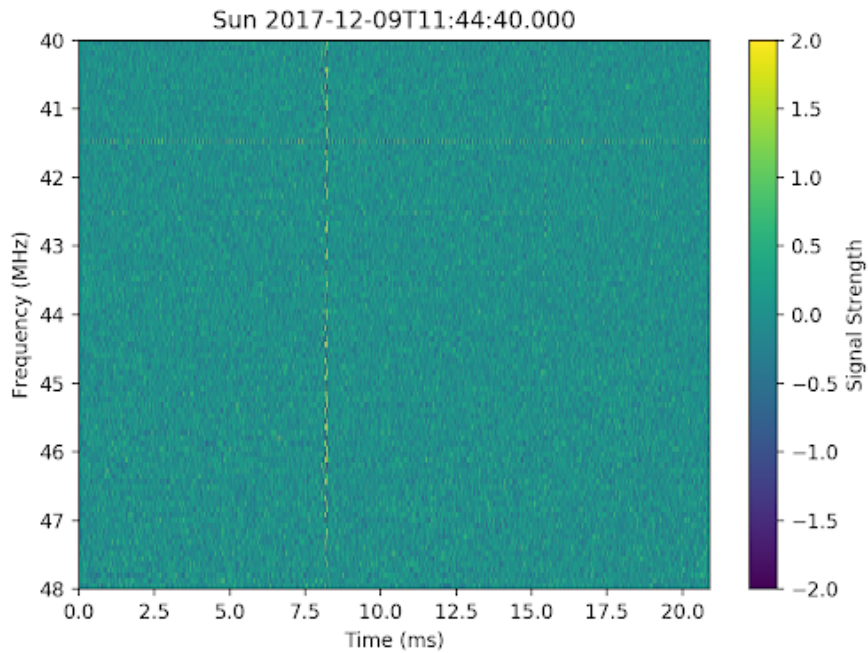


Figure 4.1: A prototype TBB dynamic spectrum created using code written in the first few months of this PhD.

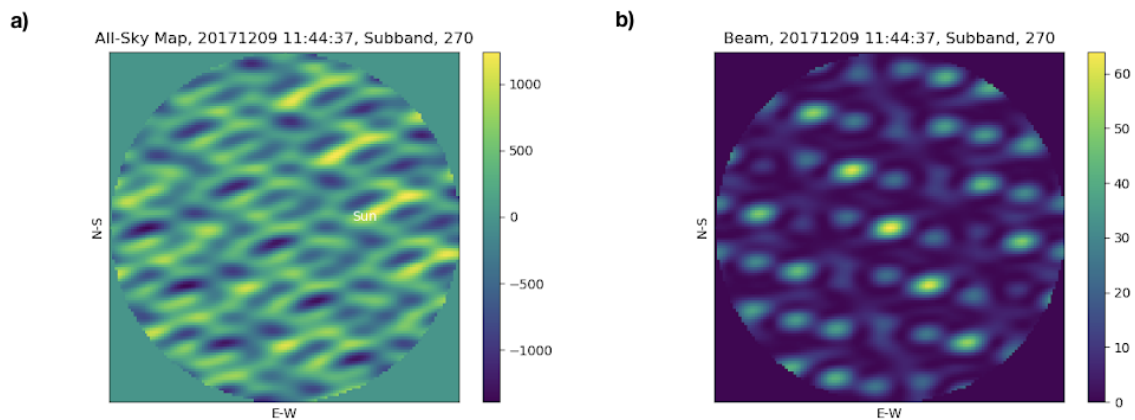


Figure 4.2: a) A prototype all sky image made from TBB data. Technical difficulties in recording data with a precise start time meant that only data from 7 antennae could be correlated to produce this image. This resulted in the point spread function b) containing numerous sidelobes.

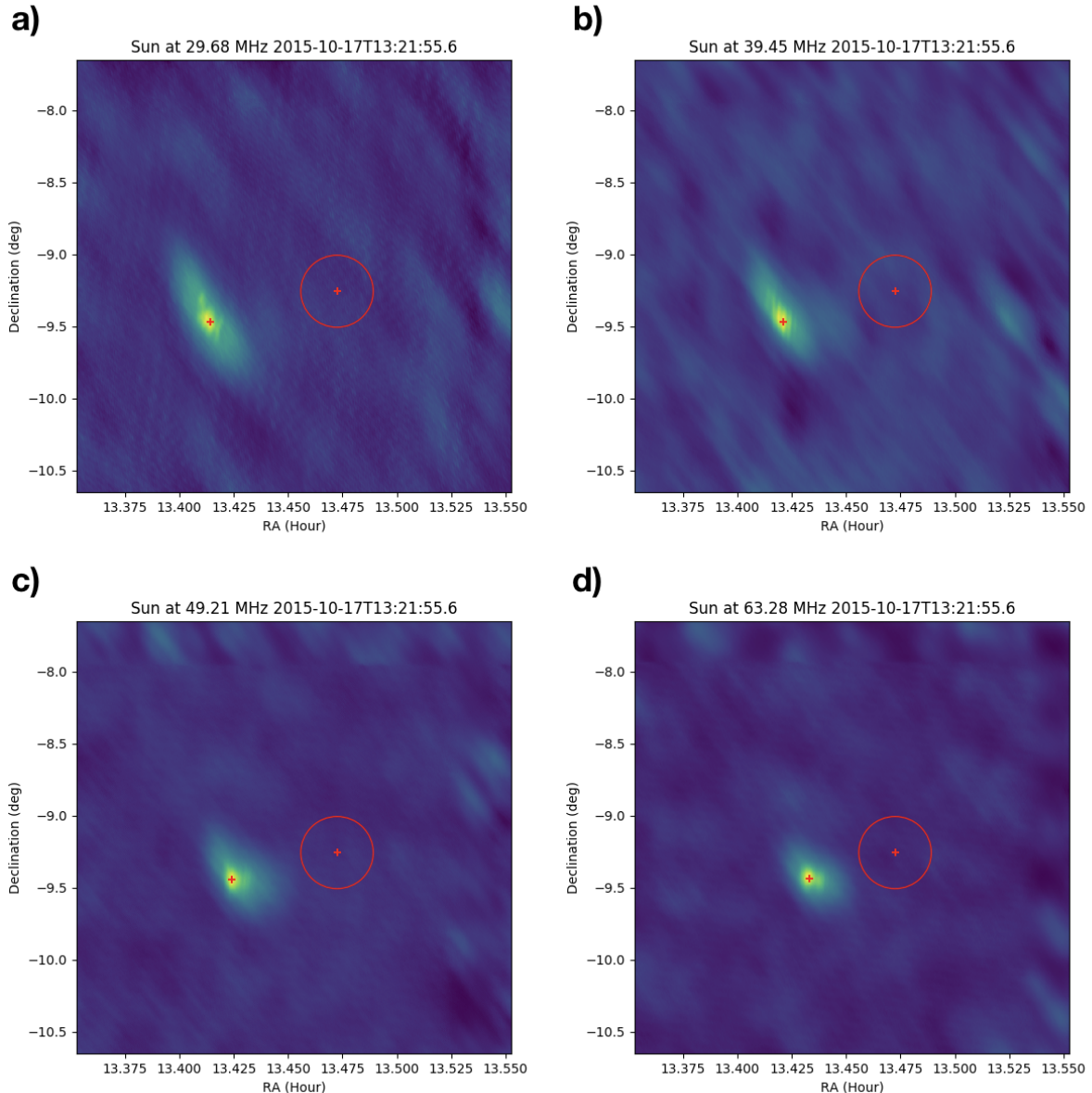


Figure 4.3: Interferometric images of a Type III burst at 13:21:55.6 on 2015-10-17 at 4 different frequencies a) 29.68 MHz b) 39.45 MHz c) 49.21 MHz d) 63.28 MHz. The red circle in each panel indicates the size of the Sun and the two red crosses indicate the centre position of the Sun and the position of maximum intensity in each panel.

The images created thus far have yet to undergo a thorough analysis of the effects of parameters used in the WSCLEAN algorithm. Different weighting schemes priorities different spatial scales in interferometric observations. Knowing that coronal scattering may effect observed source sizes, extreme care must be taken before any conclusive inferences are drawn from images produced. An initial inspection of Figure 4.3 suggests the source size of the Type III burst to be of the order of the size of the Sun at lower frequencies and $\sim 1 R_{\odot}$ at higher frequencies.

Conclusion

The solar corona produces a number of radio phenomena, some of which well understood others less so. The resolution at which the Sun can be observed in metric wavelengths has increased dramatically over the last 20 years both spatially and temporally. Current generation radio interferometers such as LOFAR offer sub arcminute spatial resolution when imaging and can produce spectra with temporal resolutions $5.12 \mu\text{s}$. The use of I-LOFAR in single station mode allows us access to an additional data recording source, the Transient Buffer Boards which can store raw voltage data at a temporal resolution of 5 ns. Software has been written to not only create spectra from this data but also to “point” I-LOFAR at a position on the sky in post processing. Two computer clusters located in the I-LOFAR control room at the Rosse Observatory, Birr Co. Offaly, act as recording and data analysis machines for data from I-LOFAR’s Remote Station Processing boards (RSPs) and TBBs. Both clusters are currently in an operational state however additional set up needs to be carried out to parallelise recording and analysing of data.

Interferometric data obtained from the LOFAR core and remote stations on 2015-10-17 from 08:00 UTC to 14:00 UTC is currently being analysed. During this time, at 13:21 UTC, a Type III burst occurred and can be seen in LOFAR beamformed observations (Figure 3.5). Preliminary images of this burst have been made using the WSCLEAN algorithm however an appropriate weighting scheme has yet to be decided upon. It is hoped that this analysis will shed light on the extent that scattering from density inhomogeneities in the corona has to play on the observed source sizes at metric wavelengths.

Future Work

The future work of this PhD can be divided into 3 main topics; technical work with REALTA and TACl, analysis of fine spatial structure in a complex radio burst, and radio frequency interference (RFI) removal using machine learning.

6.1 Technical Work

Both REALTA and TACl are operational in a minimal sense with plenty to be done to develop them as bona fide telescope backends. TACl in particular has had problems recording TBB data accurately and work is being done with Dr. Brian Coghlan of the School of Computer Science and Statistics in order to rectify this. Once operational, TACl will be able to record TBB data again and the development of software to analyse this data will be continued. It is expected that some sort of solar radio phenomenon will be detected by the TBBs and analysed before the end of this PhD.

REALTA too requires further setup before it can be used as a parallel GPU based cluster. A headnode to control the cluster operations was installed in November 2018 and collaboration with Griffin Foster (Oxford, Berkeley, Breakthrough) will continue in order to write GPU based code for data capture and analysis. The possibility of spending a week or two with Griffin is still viable.

6.2 Interferometric Analysis

Analysis of the burst event described in section 3.2 will continue and be presented at an international conference by late summer 2019. It is hoped that this analysis will shed light on the question of how much scattering effects radio propagation in the corona.

There are a number of steps that must be carried out before this can be done however, the most immediate of which is to account for the change in coordinate systems from topocentric (from the viewers perspective) to heliocentric (centered on the Sun). This will allow close comparison of radio and other wavelength observations, e.g. EUV data from AIA, as this is the standard coordinate system used in solar physics.

The imaging of this event must also be thoroughly investigated as a change in the parameters used in the WSCLEAN algorithm (Offringa et al., 2014) can result in drastically different images. As such, weighting schemes, number of iterations and more must be considered with great thought before data analysis of images can begin.

Once images have been created, the spatial scale and distance from the centre of the Sun will be measured in order to obtain a measure on how much propagation effects in the corona effect the measurement.

6.3 RFI Removal

A new method of radio frequency interference (RFI) removal will be developed using machine learning algorithms inspired by a transient detection system described by Sedaghat & Mahabal (2018). Currently this project is in its early stage but is outlined as follows. Approximately 100000 LOFAR spectra are simulated with and without RFI. These spectra will be fed into what is known as a convolutional encoder-decoder network or convolutional autoencoder (CAE) which will learn how to remove RFI without the need for a pre-made algorithm based on the physics of RFI, such as spectral kurtosis RFI removal described by Nita et al. (2007). CAEs are based on the principals of autoencoders described in Vincent et al. (2008) but using the convolutional methods that have seen great success in image processing.

References

- Appleton, E. & Hey, J. 1946, The London, Edinburgh, and Dublin Philosophical Magazine and Journal of Science, 37, 73 5
- Aschwanden, M. J. 2004, Physics of the Solar Corona 3
- Bastian, T. S. 1994, The Astrophysical Journal, 426, 774 5
- Boischot, A. & André. 1957, Comptes Rendus de l'Académie des Sciences, Paris, Vol. 244, p. 1326-1329, 244, 1326 5
- Broekema, P. C., Mol, J. J. D., Nijboer, R., et al. 2018 13
- Clarke, B. P., Morosan, D. E., Gallagher, P. T., et al. 2019 4
- Dulk, G. A. 1985, Annual Review of Astronomy and Astrophysics, 23, 169 4
- Ellis, G. 1969, Australian Journal of Physics, 22, 177 4
- Foukal, P. V. 2004, Solar Astrophysics, 480 1
- Ginzburg, V. L. & Zhelezniakov, V. V. 1958, Astronomicheskii Zhurnal, 35, 694 5, 6, 10
- Kontar, E. P., Yu, S., Kuznetsov, A. A., et al. 2017, Nature Communications, 8, 1515 5
- Malville, J. M. & M., J. 1962, The Astrophysical Journal, 135, 834 5
- McCauley, P. I., Cairns, I. H., Morgan, J., et al. 2017, The Astrophysical Journal, 851, 151 22
- McConnell, D. 1980, Publications of the Astronomical Society of Australia, 4, 64 4, 5
- McLean, D. J. & Labrum, N. R. 1985, Cambridge and New York, Cambridge University Press, 1985, 527 p. For individual items see A87-13852 to A87-13867. 5
- Melnik, V. N., Konovalenko, A. A., Rucker, H. O., et al. 2010, Solar Physics, 264, 103 4
- Melrose, D. B. 1982, Solar Radio Storms, CESRA Workshop #4, 182 4
- Melrose, D. B. 1987, Solar Physics, 111, 89 8
- Mitalas, R. & Sills, K. R. 1992, The Astrophysical Journal, 401, 759 1
- Morosan, D. E., Gallagher, P. T., Zucca, P., et al. 2014, Astronomy & Astrophysics, 568, A67 22
- Morosan, D. E., Gallagher, P. T., Zucca, P., et al. 2015, Astronomy & Astrophysics, 580, A65 4
- Nelson, G. J. & Melrose, D. B. 1985, in Solar Radiophysics: Studies of Emission from the Sun at Metre Wavelengths, ed. D. J. McLean & N. R. Labrum, 333–359 4
- Nita, G. M., Gary, D. E., Liu, Z., Hurford, G. J., & White, S. M. 2007, Publications of the Astronomical Society of the Pacific, 119, 805 33
- Offringa, A. R., McKinley, B., Hurley-Walker, N., et al. 2014, Monthly Notices of the Royal Astronomical Society, 444, 606 32
- Reid, H. A. S. & Kontar, E. P. 2017 7
- Reid, H. A. S. & Ratcliffe, H. 2014, Research in Astronomy and Astrophysics, 14, 773 6, 9
- Riddle, A. C. 1974, Solar Physics, 35, 153 5
- Sedaghat, N. & Mahabal, A. 2018, Monthly Notices of the Royal Astronomical Society, 476, 5365 33
- Turck-Chièze, S. & Couvidat, S. 2011, Reports on Progress in Physics, 74, 086901 1
- van Haarlem, M. P., Wise, M. W., Gunst, A. W., et al. 2013, Astronomy & Astrophysics, Volume 556, id.A2, 53 pp., 556 5, 13
- Vedenov, A. A. 1963, Journal of Nuclear Energy. Part C, Plasma Physics, Accelerators, Thermonuclear Research, 5, 169 8
- Vincent, P., Larochelle, H., Bengio, Y., & Manzagol, P.-A. 2008, in Proceedings of the 25th international conference on Machine learning - ICML '08 (New York, New York, USA: ACM Press), 1096–1103 33
- Wild, J. P. 1950, Australian Journal of Chemistry, 3, 399 4
- Wild, J. P. & McCready, L. L. 1950, Australian Journal of Scientific Research A, vol. 3, p.387, 3, 387 5
- Wild, J. P., Sheridan, K. V., & Trent, G. H. 1959, URSI Symp. 1: Paris Symposium on Radio Astronomy, 9, 176 5
- Zucca, P., Carley, E. P., McCauley, J., et al. 2012, Solar Physics, 280, 591 vi, 6, 7

A

Appendix

Insert Appendix here